Check for updates

Geophysical Research Letters

RESEARCH LETTER
10.1029/2024GL112450

Multi-Frequency SuperDARN HF Radar Observations of the Ionospheric Response to the October 2023 Annular Solar Eclipse

E. G. Thomas[1], S. G. Shepherd[1], B. S. R. Kunduri[2], and D. R. Themens[3]

[1]Dartmouth College, Hanover, NH, USA, [2]Virginia Tech, Blacksburg, VA, USA, [3]University of Birmingham, Birmingham, UK

Key Points:

- A novel multi-frequency experiment was conducted with the Christmas Valley East SuperDARN radar during the 14 October 2023 annular eclipse
- Our comparison with the nearby Boulder Digisonde shows a strong correlation in 1-hop skip distance with F2-layer critical frequency
- The transition from negative to positive Doppler shifts is clearly aligned with the time derivative of eclipse shadow

Supporting Information:

Supporting Information may be found in the online version of this article.

Correspondence to:

E. G. Thomas,
evan.g.thomas@dartmouth.edu

Citation:

Thomas, E. G., Shepherd, S. G., Kunduri, B. S. R., & Themens, D. R. (2024). Multi-frequency SuperDARN HF radar observations of the ionospheric response to the October 2023 annular solar eclipse. *Geophysical Research Letters*, *51*, e2024GL112450. https://doi.org/10.1029/2024GL112450

Received 13 SEP 2024
Accepted 5 NOV 2024

© 2024. The Author(s).
This is an open access article under the terms of the Creative Commons Attribution-NonCommercial-NoDerivs License, which permits use and distribution in any medium, provided the original work is properly cited, the use is non-commercial and no modifications or adaptations are made.

Abstract An annular solar eclipse was visible on 14 October 2023 from 15:00–21:00 UT as its path traveled across North, Central, and South America. In this letter, we present the first multi-frequency Super Dual Auroral Radar Network (SuperDARN) observations of the bottomside ionospheric response to a solar eclipse using a novel experimental mode designed for the October 2023 annular eclipse. We compare our results from the mid-latitude Christmas Valley East radar with measurements of the vertical electron density profile from the nearby Boulder Digisonde, finding the changes in 1- and 2-hop ground scatter skip distance are well correlated with the F_2-layer density response, which lags the peak obscuration by ~30 min. Changes in the line-of-sight Doppler shifts are better aligned with the time derivative of eclipse obscuration.

Plain Language Summary During a solar eclipse when the moon passes between our planet and the sun, the amount of incoming solar extreme ultraviolet radiation is reduced over the shadowed region of Earth. As a result, temperatures can become cooler and the rate of plasma production in the ionized layers of the Earth's upper atmosphere, known as the ionosphere, can also decrease. Users of high-frequency radio systems, such as over-the-horizon radar and amateur radio, depend on knowledge of the ionospheric plasma density, and are therefore susceptible to abrupt changes due to space weather phenomena such as a solar eclipse. While not attracting as much media attention as the total solar eclipses over North America in August 2017 and April 2024, the annular solar eclipse of October 2023 nevertheless presented a unique opportunity to study the response of Earth's upper atmosphere using a diverse array of ground-based instruments in a similar region but at a different time of day. For this event, we designed a new experimental mode for a pair of space weather radars located in central Oregon to transmit signals at a range of frequencies in the HF band to monitor their evolution as the eclipse shadow passed nearby.

1. Introduction

Solar eclipses are rare space weather events in which the sun's ionizing extreme ultraviolet (EUV) radiation is obscured by the moon from reaching Earth's upper atmosphere, directly impacting the photochemical production processes in the lower E- and F_1-layers of the ionosphere. There is also a reduction in EUV-associated heating, which modifies the thermospheric neutral winds and therefore electron densities at higher altitudes in the F_2-region where transport processes play a more significant role (e.g., Cnossen et al., 2019; Müller-Wodarg et al., 1998; Rishbeth, 1968; Salah et al., 1986). Many of the earliest studies of the Earth's environmental response to solar eclipses use observations from high-frequency (HF) radio instruments like vertical incidence ionosondes and oblique HF Doppler sounders, identifying common features such as a reduction in the electron density and bipolar HF Doppler shifts (Cornelius & Essex, 1978; Evans, 1965; Hanuise et al., 1982). However, subsequent modeling and observational studies have demonstrated the coupled ionosphere-thermosphere response is highly dependent on solar activity, season, local time (LT), latitude, etc (e.g., Chernogor et al., 2022; Grigorenko et al., 2008; Guo et al., 2020; Jakowski et al., 2008; Jones et al., 2004; Le et al., 2008; Mosna et al., 2018; Sindelarova et al., 2018; Vertogradov & Vertogradova, 2016).

The Super Dual Auroral Radar Network (SuperDARN) is an international collaboration of more than 30 ground-based, HF radars continuously operating in both the Northern and Southern Hemispheres (Chisham et al., 2007; Greenwald et al., 1985, 1995; Nishitani et al., 2019). By utilizing the refraction of HF radio waves as they propagate obliquely through the bottomside ionosphere, SuperDARN radars can measure the line-of-sight (LOS) Doppler velocity of backscatter echoes from field-aligned plasma irregularities to monitor large-scale plasma

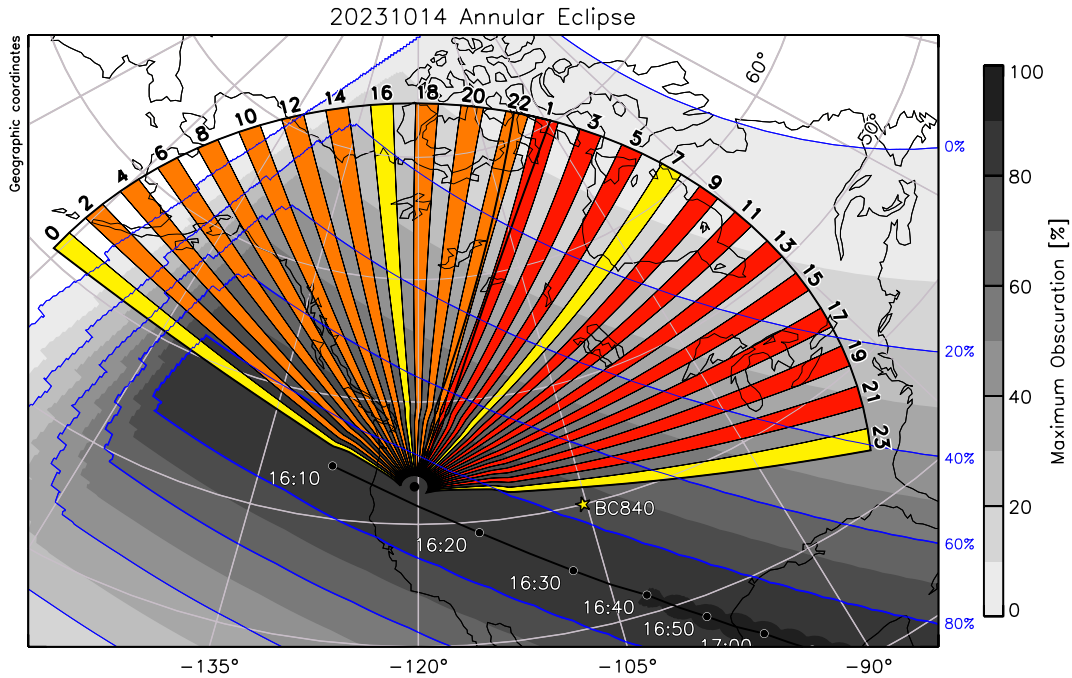

Figure 1. Nominal fields of view of the Christmas Valley East and West SuperDARN radars shaded red and orange, respectively, during a special multi-frequency experiment for the annular solar eclipse on 14 October 2023, plotted in geographic coordinates; beams highlighted in yellow sampled nine equally spaced frequencies from 9.5 to 17.5 MHz each minute. Contours of maximum obscuration at 300 km altitude are overlaid in gray with 20% contour intervals marked in blue (Frissell, N. A., 2023). The Boulder Digisonde (BC840) is indicated by the yellow star.

motion at *E*- and *F*-region altitudes. In the presence of a dense enough layer, the transmitted radio waves can be fully refracted back toward the ground to produce backscatter echoes from the Earth's land and sea surfaces.

Despite the radar network's long history spanning more than three decades, only one published work has examined SuperDARN measurements during an eclipse. Moses et al. (2021) present SuperDARN observations from the 21 August 2017 total solar eclipse over North America, finding an increase in the skip distance of the 1-hop ground scatter and a reduction in the total amount of backscatter seen by the mid-latitude Fort Hays West (FHW) and Christmas Valley West (CVW) radars. The response observed by CVW was symmetric about the time of maximum obscuration, while the FHW observations were asymmetric with the recovery time lasting longer than the onset phase. More recently, another total solar eclipse occurring over North America on 8 April 2024 was observed by the mid-latitude Blackstone (BKS) radar and is described in the companion paper (Kunduri et al., 2024). In this letter, we present the first multi-frequency SuperDARN radar observations of the ionospheric response to a solar eclipse; specifically, the annular solar eclipse occurring over North America on 14 October 2023.

2. Methodology and Data

In this study, we use data from the Christmas Valley East (CVE) SuperDARN radar in Oregon (43.27° N, 120.36° W), which forms a co-located pair with CVW. From 15:00–20:00 UT on 14 October 2023, the Christmas Valley radars were operated in a special mode that samples every other beam at a single frequency (10.6 MHz) during the first 30 s of each 1-min scan. In the remaining 30 s, the radars scan through nine frequencies (9.5–17.5 MHz) along two selected beam directions (7 and 23 for CVE; 0 and 16 for CVW). Figure 1 shows the nominal fields of view (FOVs) of each radar in geographic coordinates, with red and orange shading used to indicate the single-frequency beams sampled by CVE and CVW, respectively; the four multi-frequency beams are shaded yellow. LOS Doppler velocities are obtained from the raw data samples using the FITACF 2.5 library contained in version 5.0 of the Radar Software Toolkit (RST) (SuperDARN Data Analysis Working Group et al., 2022).

Contours of maximum obscuration at 300 km altitude during the eclipse are overlaid on Figure 1 in gray, with 20% contour intervals marked by solid blue lines (Frissell, N. A., 2023). The center of the eclipse path is indicated by

19448007, 2024, 24, Downloaded from https://agupubs.onlinelibrary.wiley.com/doi/10.1029/2024GL112450, Wiley Online Library on [12/12/2024]. See the Terms and Conditions (https://onlinelibrary.wiley.com/terms-and-conditions) on Wiley Online Library for rules of use; OA articles are governed by the applicable Creative Commons License

10.1029/2024GL112450

19448007, 2024, 24, Downloaded from https://agupubs.onlinelibrary.wiley.com/doi/10.1029/2024GL112450, Wiley Online Library on [12/12/2024]. See the Terms and Conditions (https://onlinelibrary.wiley.com/terms-and-conditions) on Wiley Online Library for rules of use; OA articles are governed by the applicable Creative Commons License

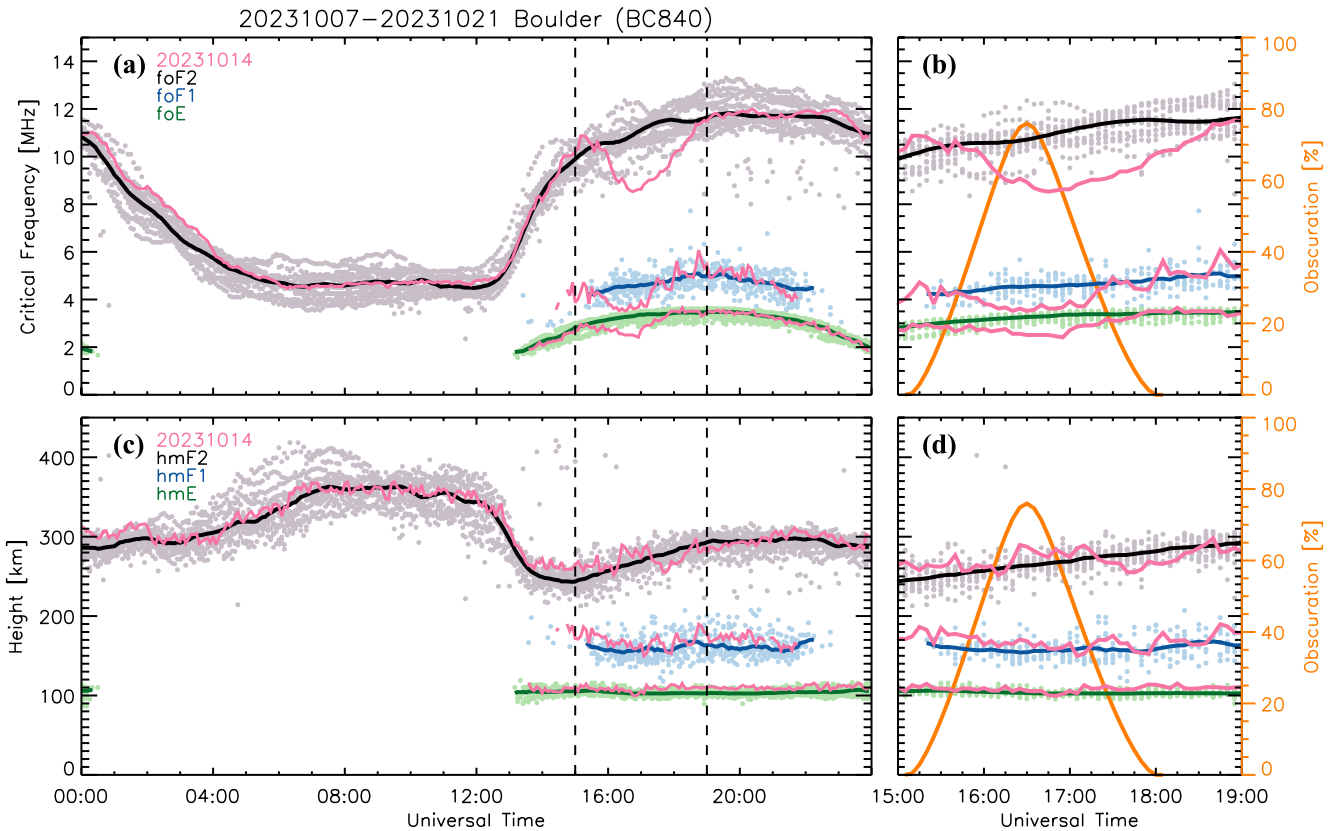

Figure 2. Boulder Digisonde (BC840) measurements of (a–b) critical frequency and (c–d) layer height at a 5 min cadence. Light green, blue, and gray dots indicate E, F_1, and F_2-layer measurements during the week before and after the annular solar eclipse, respectively; thick green, blue, and black lines correspond to smoothed median values for each layer. The solid pink lines show the measured layer values on the eclipse day. Vertical dashed lines in panels (a, c) indicate the expanded 4-hr time interval shown in panels (b, d), where the eclipse obscuration at 300 km altitude is overlaid in orange.

the solid black line and labeled at 10-min intervals starting from 16:10 UT. While totality (i.e., 100% obscuration) does not occur anywhere within the radars' FOV, the radar site does lie within the band of 80%–90% maximum obscuration and is only a few degrees poleward of the shadow center as it passes by at 16:15 UT. CVE's two multi-frequency beams (7 and 23) look nearly perpendicular and parallel to the central eclipse path; therefore, we focus on observations from CVE due to its more favorable viewing geometry relative to the eclipse.

We use data from the nearby Boulder Digisonde (BC840) to characterize the ionospheric vertical electron density profile (Bibl & Reinisch, 1978). Daily autoscaled results for the week before and after the eclipse at 5 min cadence are obtained from the Lowell Digital Ionogram DataBase (Reinisch & Galkin, 2011) to calculate median reference values, while we have manually scaled the ionogram for the eclipse day. The geographic location of BC840 (40.0° N, 105.7° W) is indicated by the yellow star overlaid on Figure 1.

3. Observations

The maximum obscuration at 300 and 100 km altitude over Boulder were 76.0% and 77.5%, occurring at 16:30 and 16:35 UT, respectively. Figure 2 shows a 24-hr time series of (a) critical frequency and (b) peak height of the E, F_1, and F_2 layers observed by BC840 on the eclipse day as solid pink lines. Lighter colored dots show individual measurements of each layer parameter during the week before and after from 07 to 21 October 2023 (excluding the eclipse day), while the thick green, blue, and black lines correspond to median values. In Figure 2a, the pink eclipse day critical frequencies match the 14-day medians quite closely, except from ~15:00–19:00 UT when the eclipse shadow was passing nearby. Figure 2b shows an expanded view of this 4-hr interval with the obscuration above Boulder at 300 km overlaid in orange. The critical frequencies of all three layers begin decreasing at 15:20 UT and reach a local minimum at 16:45 UT, corresponding to a reduction of ~20% and lagging the obscuration peak at 300 km altitude by 15 min. The E (foE) and F_1 (foF1) layer critical frequencies

10.1029/2024GL112450

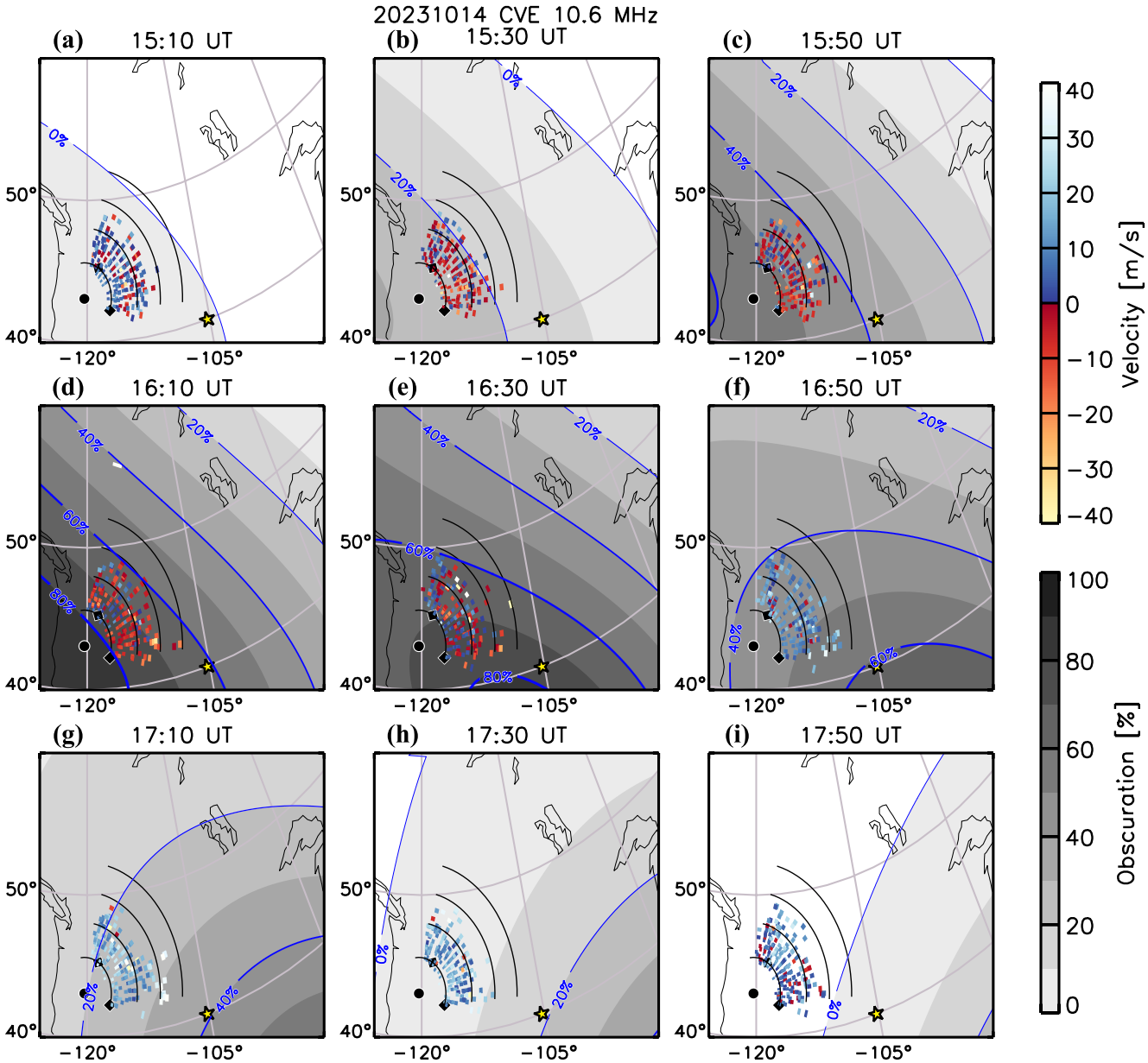

Figure 3. Fitted line-of-sight Doppler velocity measurements from Christmas Valley East at 10.6 MHz from (a–i) 15:10–17:50 UT at 20 min intervals on 14 October 2023, mapped to the ionospheric reflection point using measured elevation angles and assuming 1-hop propagation. Contours of eclipse obscuration at 300 km altitude are overlaid on each panel, with contours at 20% intervals marked in blue; locations of obscuration values in Figure 5 are indicated by black diamonds. The location of BC840 is indicated by the yellow star.

both recover to their median values within the next 60 min by 18:00 UT, while the F_2 critical frequency (foF2) does not reach its median value until 18:40 UT. In Figures 2c and 2d, no significant deviations from the median layer heights are observed during the eclipse, with two exceptions. Likely signatures of traveling ionospheric disturbances (TIDs) can be seen in both the F_1-layer height (hmF1) and foF1 after the eclipse maximum from 17:30–19:00 UT. There is also a slight increase in the F_2 layer height (hmF2) by ~20 km at 16:25 UT, although it is within the range of daily observed values (gray dots).

Observations of daytime ground backscatter from CVE give insight into the spatial and temporal evolution of the bottomside ionosphere during the eclipse. Figure 3 shows fitted LOS Doppler velocity measurements for the single-frequency CVE beams (i.e., red beams in Figure 1) from 15:10–17:50 UT at 20 min intervals. The measured range and elevation angles are used to map the backscatter echoes to their ionospheric reflection point

19448007, 2024, 24, Downloaded from https://agupubs.onlinelibrary.wiley.com/doi/10.1029/2024GL112450, Wiley Online Library on [12/12/2024]. See the Terms and Conditions (https://onlinelibrary.wiley.com/terms-and-conditions) on Wiley Online Library for rules of use; OA articles are governed by the applicable Creative Commons License

19448007, 2024, 24, Downloaded from https://agupubs.onlinelibrary.wiley.com/doi/10.1029/2024GL112450, Wiley Online Library on [12/12/2024]. See the Terms and Conditions (https://onlinelibrary.wiley.com/terms-and-conditions) on Wiley Online Library for rules of use; OA articles are governed by the applicable Creative Commons License

assuming a 1-hop propagation mode (Thomas & Shepherd, 2022); solid black lines are overlaid every 10 range gates assuming a fixed virtual reflection height of 300 km for reference. Similar to Figure 1, obscuration contours at 300 km altitude for each time step are overlaid in gray and BC840 is indicated by the yellow star. At 15:10 UT (Figure 3a), when the 0%–10% obscuration contour covers both the CVE backscatter reflection points and BC840, the observed LOS velocities are a mixture of small positive and negative values (±10 m/s). As the eclipse shadow approaches CVE over the next 60 min (Figures 3b–3d) the LOS velocities become consistently negative (as indicated by the predominantly red colors), until the footprint has passed equatorward of the radar at 16:30 UT (Figure 3e) when more positive velocities (predominantly blue colors) begin to appear again. Over the next 60 min as the eclipse travels farther away from the radar to the southeast (Figures 3f–3i), the velocities are consistently positive.

In addition to the single-frequency results obtained across the entire CVE FOV, oblique multi-frequency data were collected along beams 7 and 23 to monitor the downrange bottomside ionospheric response to the eclipse. Figure 4 shows range-time intensity plots of the LOS Doppler velocity observed along beam 23 of CVE at the nine sounding frequencies (9.5–17.5 MHz at 1 MHz steps) from 15:00–19:00 UT using the same velocity scale as Figure 3. The solid white line indicates the smoothed skip distance of the 1-hop ground scatter observed at each frequency, and the dashed white line corresponds to twice this distance as an estimate for any possible 2-hop ground scatter. Overlaid on each panel of Figure 4 in black is the foF2 measured by BC840.

In all panels of Figure 4, the skip distance begins increasing by a few hundred kilometers at ∼15:30 UT until 16:45–17:00 UT, after which it decreases back to the initial measured slant range by 17:45–18:00 UT. The 2-hop skip distance estimate (dashed white line) tends to closely follow the near range of a farther ground scatter band during the initial phase of increasing skip distance, however an offset of ∼100 km is observed during the subsequent recovery phase. The LOS Doppler velocities are mostly negative from ∼15:30–16:30 UT, followed by mostly positive velocities until 18:00 UT. The velocity magnitudes also appear to be inversely proportional to radar frequency. Cross-correlation analysis indicates foF2 is strongly anti-correlated with the 1-hop skip distances at each frequency (−0.85 to −0.90), but the times of skip distance maximum span from 10 min before the minimum in foF2 at the lowest frequency (9.5 MHz) to 15 min after for the higher frequencies (13.5–17.5 MHz).

CVE's other multi-frequency beam (7) is directed nearly perpendicular to the eclipse path, and its observations are largely similar to those along beam 23 shown in Figure 4; an equivalent figure is available in the Supporting Information S1. The 1-hop skip distance at each frequency along beam 7 is again strongly anti-correlated with foF2, which lags the skip distance maximum by 5 min. Unlike beam 23, there appears to be some periodic structure in the observed Doppler velocities embedded within the ground scatter's overall trend from negative to positive values.

4. Discussion and Summary

In this letter we have presented the first multi-frequency SuperDARN HF radar observations of the ionospheric response to a solar eclipse. Unlike the August 2017 total solar eclipse described by Moses et al. (2021), the 1-hop ground scatter band remained visible at all radar operating frequencies throughout the October 2023 annular eclipse. Negative LOS Doppler velocities and increasing skip distance were observed in the 1-hop ground backscatter as the eclipse shadow approached the CVE radar's FOV, followed by positive Doppler velocities and decreasing skip distance as the obscuration decreased. The nearby Digisonde observed a ∼20% decrease in foE, foF1, and foF2 during the eclipse, while the peak layer heights remained relatively stable.

To better explore the relative timing of the multi-frequency SuperDARN results with respect to changes in eclipse obscuration, the top two rows of Figure 5 show the smoothed 1-hop skip distance and median Doppler velocity extracted along CVE's beams 23 and 7 in the left and right columns, respectively. The maximum skip distance along each beam is indicated by the filled circles and connected by a dotted line. Along beam 23 (Figure 5a), there is a clear time delay in the maximum skip distance moving from low to high radar frequencies between 16:35–17:00 UT, whereas along beam 7 (Figure 5b) the maximum skip distance occurs simultaneously for all frequencies at 16:39 UT. The obscuration at 300 km altitude along each beam near the skip distance reflection point (black diamonds in Figure 3) is overlaid in white. Maximum obscuration occurred nearly simultaneously at 16:15 UT for both beams, with a peak value of 86.4% along beam 23 and 79.0% along beam 7, respectively. The changes in skip distance therefore lag the peak obscuration by 20–45 min depending on both radar frequency and

10.1029/2024GL112450

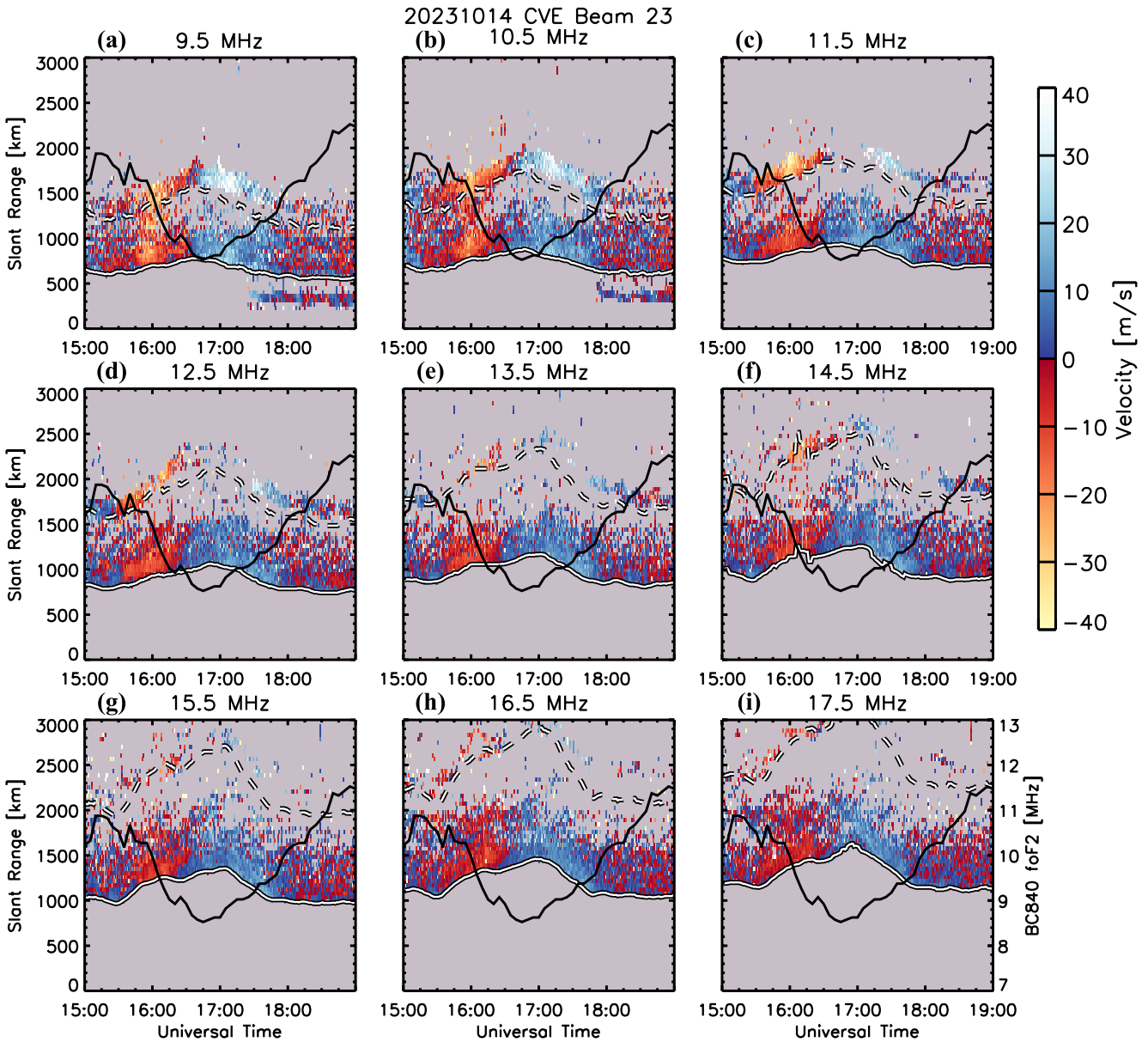

Figure 4. Fitted line-of-sight Doppler velocity measurements along CVE's beam 23 at nine frequencies as a function of measured slant range from 15:00–19:00 UT on 14 October 2023. The smoothed 1-hop skip distance is overlaid as a solid white line, and the dashed white line indicates twice this range as a prediction of the 2-hop skip distance. BC840 measurements of the F_2-layer critical frequency (foF2) are overlaid in black.

azimuthal beam direction (noting that beam 23 is more parallel and beam 7 more perpendicular to the eclipse path).

The Doppler velocities shown in Figures 5c and 5d reveal values are negative or zero prior to ~16:15 UT, after which positive values are observed along both beams at all frequencies. The velocity magnitudes have a clear frequency dependence with the largest values observed at lower frequencies, which is expected given the relationship between Doppler velocity (v_D) and the Doppler frequency shift (Δf) obtained from the autocorrelation function and given by

$$v_D = \frac{c\Delta f}{2f_0} \quad (1)$$

19448007, 2024, 24, Downloaded from https://agupubs.onlinelibrary.wiley.com/doi/10.1029/2024GL112450, Wiley Online Library on [12/12/2024]. See the Terms and Conditions (https://onlinelibrary.wiley.com/terms-and-conditions) on Wiley Online Library for rules of use; OA articles are governed by the applicable Creative Commons License

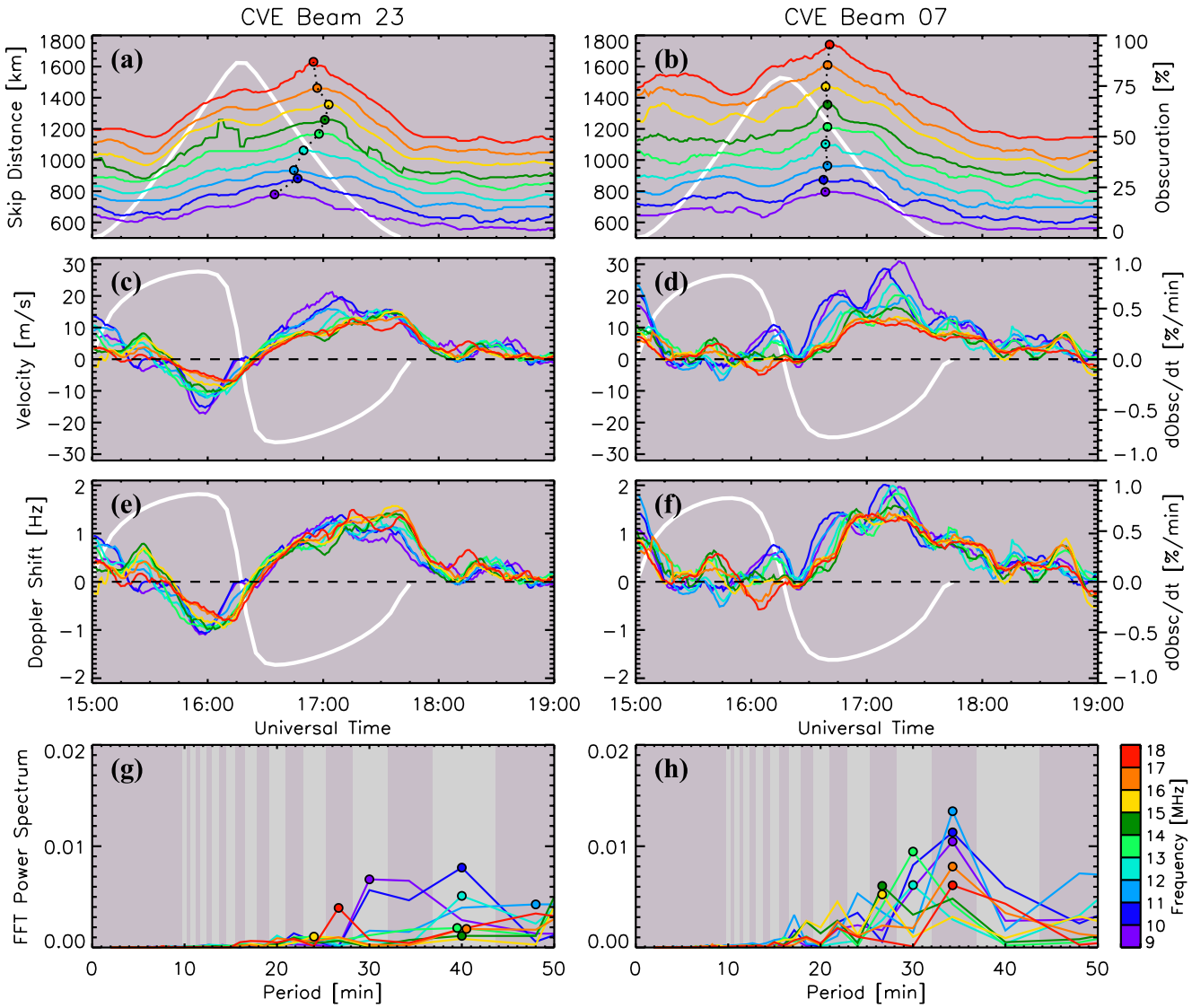

Figure 5. Christmas Valley East observations along beam 23 (left) and beam 7 (right) of smoothed (a–b) 1-hop skip distance, (c–d) line-of-sight Doppler velocity, and (e–f) Doppler frequency shift at nine frequencies from 15:00–19:00 UT on 14 October 2023. The eclipse obscuration at 300 km in the near fields of view along each beam is overlaid in white on panels (a–b), and the time derivative of the obscuration function is overlaid on panels (c–f) in white. Panels (g, h) show the fast Fourier transform power spectral density of the Doppler frequency shifts in panels (e, f), respectively.

where f_0 is the radar frequency and c is the speed of light (Baker et al., 1995; Ribeiro et al., 2013). Using Equation 1 we convert the radar velocities to their associated Doppler frequency shifts as shown in Figures 5e and 5f, where the Doppler shift magnitudes at each frequency are now much better aligned. A strong anti-correlation is found between the Doppler shifts along beam 23 and the time derivative of the eclipse obscuration at 300 km ($dObsc/dt$), which is overlaid on Figures 5c–5f in white.

Typically during the initial stage of an eclipse when occultation is increasing ($dObsc/dt > 0$), a negative Doppler shift is expected, followed by a positive Doppler shift as the occultation decreases (e.g., Chernogor et al., 2022; Sindelarova et al., 2018). The October 2023 annular eclipse was observed by CVE and BC840 in the pre-noon sector (~09:15 LT), so the expected negative Doppler shift due to increasing occultation is likely offset by the diurnal increase in electron density (Figure 2a). After the peak obscuration (16:15 UT), the decreasing obscuration ($dObsc/dt < 0$) and increasing electron density due to daytime production processes should both generate a positive Doppler shift. The largest negative Doppler shifts were observed along CVE's beam 23, which is most parallel to the eclipse path, while the negative Doppler shift along the perpendicular beam 7 was almost totally

19448007, 2024, 24, Downloaded from https://agupubs.onlinelibrary.wiley.com/doi/10.1029/2024GL112450, Wiley Online Library on [12/12/2024]. See the Terms and Conditions (https://onlinelibrary.wiley.com/terms-and-conditions) on Wiley Online Library for rules of use; OA articles are governed by the applicable Creative Commons License

19448007, 2024, 24, Downloaded from https://agupubs.onlinelibrary.wiley.com/doi/10.1029/2024GL112450, Wiley Online Library on [12/12/2024]. See the Terms and Conditions (https://onlinelibrary.wiley.com/terms-and-conditions) on Wiley Online Library for rules of use; OA articles are governed by the applicable Creative Commons License

suppressed. Because BC840 did not observe significant changes in layer height in response to the eclipse, we believe the large-scale Doppler shifts are more likely attributable to time changes in the bottomside electron density (e.g., equation 8 in Chum et al. (2012)).

Interpretation of the Doppler shifts along CVE's beam 7 are complicated by wave activity, which is clearly seen throughout this interval in Figure 5f. A nearly 180° phase shift is observed between the lowest and highest frequencies from 15:30-16:30 UT, suggesting each frequency corresponds to a different downrange ionospheric reflection point as the disturbances propagate away from the eclipse path (e.g., Zhang et al., 2017). TIDs are also known to exhibit phase variations at different altitudes, and so the reflection height at each frequency may play a significant role (e.g., Panasenko et al., 2019). The bottom row of Figure 5 shows the fast Fourier transform (FFT) power spectral density of the Doppler frequency shifts along each beam. A clear peak at 35 min is seen in the FFT power spectrum for beam 7 (Figure 5h), whereas a smaller, broader range spanning from 25 to 45 min is found for beam 23 (Figure 5g). Unfortunately, limited ground backscatter was observed prior to 15:00 UT making it difficult to determine whether this wave activity preceded the eclipse. We do note that BC840 also observed TID-like signatures in the F_1-layer for 1.5 hr after the obscuration maximum.

The experimental setup between the October 2023 annular eclipse described in this letter and the April 2024 total eclipse described in the companion paper (Kunduri et al., 2024) are quite similar, with a mid-latitude SuperDARN radar observing changes in the 1-hop ground scatter skip distance and Doppler velocity sign near a Digisonde providing vertical electron density profile measurements. However, several important differences should be noted. First, the October annular eclipse reached CVE at ~16:15 UT in the pre-noon sector (~09:15 LT), whereas the April total eclipse did not reach the Digisonde deployed under the BKS radar FOV until several hours later at 19:30 UT (~15:30 LT). During both events foE and foF1 responded nearly instantly to the eclipse shadow, while during the April eclipse the foF2 response lagged the other layers by ~45 min. Because of foF2's simultaneous response during the October 2023 eclipse, we are unable to attribute the observed Doppler shifts to a particular layer; the changes in skip distance however appear best correlated with foF2.

To summarize, the novel multi-frequency experiment conducted with the CVE SuperDARN radar during the October 2023 annular solar eclipse provides key spatial context to nearby vertical incidence measurements of the bottomside ionosphere. In our future work, we will expand our analysis to include multi-frequency data from other radars and eclipses to further characterize the ionospheric response to these unique space weather events.

Data Availability Statement

The authors acknowledge the use of SuperDARN data. SuperDARN is a collection of radars funded by the national scientific funding agencies of Australia, Canada, China, France, Italy, Japan, Norway, South Africa, United Kingdom, and the United States of America. The raw SuperDARN data used in this study have been uploaded to Zenodo (Thomas et al., 2024). The Radar Software Toolkit to read and process the SuperDARN data can be downloaded from Zenodo (SuperDARN Data Analysis Working Group et al., 2022). The Boulder Digisonde (BC840) was operated by University of Colorado Boulder on behalf of the National Oceanic and Atmospheric Administration and data were obtained from the Lowell Digital Ionogram DataBase, DIDBase (https://giro.uml.edu/didbase/) at the Lowell GIRO Data Center, LGDC (Reinisch & Galkin, 2011). Manually scaled ionogram parameters from BC840 for the day of the eclipse have also been uploaded to Zenodo (Thomas et al., 2024). The eclipse obscuration contours were obtained from Frissell, N. A. (2023).

Acknowledgments

This research was funded by the Office of Naval Research (ONR) under Grant N000142312109, Air Force Research Laboratory under Grant FA94532220027, and National Science Foundation (NSF) under Grant AGS-1934997. BSRK acknowledges support from NASA under Grants 80NSSC23K1321 and 80NSSC22K1635, and from NSF under Grant AGS-1935110. DRT's contributions to this work are supported by ONR PRISM Grant N00014-23-S-B001 and by the UK Met Office ARCTIC project.

References

Baker, K. B., Dudeney, J. R., Greenwald, R. A., Pinnock, M., Newell, P. T., Rodger, A. S., et al. (1995). HF radar signatures of the cusp and low-latitude boundary layer. *Journal of Geophysical Research*, *100*(A5), 7671–7695. https://doi.org/10.1029/94JA01481

Bibl, K., & Reinisch, B. W. (1978). The universal digital ionosonde. *Radio Science*, *13*(3), 519–530. https://doi.org/10.1029/RS013i003p00519

Chernogor, L. F., Garmash, K. P., Guo, Q., Rozumenko, V. T., & Zheng, Y. (2022). Ionospheric effects of the 5–6 January 2019 eclipse over the People's Republic of China: Results from oblique sounding. *Annales Geophysicae*, *40*(5), 585–603. https://doi.org/10.5194/angeo-40-585-2022

Chisham, G., Lester, M., Milan, S. E., Freeman, M. P., Bristow, W. A., Grocott, A., et al. (2007). A decade of the Super Dual Auroral Radar Network (SuperDARN): Scientific achievements, new techniques and future directions. *Surveys in Geophysics*, *28*(1), 33–109. https://doi.org/10.1007/s10712-007-9017-8

Chum, J., Hruska, F., Zednik, J., & Lastovicka, J. (2012). Ionospheric disturbances (infrasound waves) over the Czech Republic excited by the 2011 Tohoku earthquake. *Journal of Geophysical Research*, *117*(A8), A08319. https://doi.org/10.1029/2012JA017767

Cnossen, I., Ridley, A. J., Goncharenko, L. P., & Harding, B. J. (2019). The response of the ionosphere-thermosphere system to the 21 August 2017 solar eclipse. *Journal of Geophysical Research: Space Physics*, *124*(8), 7341–7355. https://doi.org/10.1029/2018JA026402

Cornelius, D. W., & Essex, E. A. (1978). HF Doppler observations of 23 October, 1976 total solar eclipse over south-eastern Australia. *Journal of Atmospheric and Terrestrial Physics*, *40*(4), 497–502. https://doi.org/10.1016/0021-9169(78)90184-8

Evans, J. V. (1965). On the behavior of f_0F_2 during solar eclipses. *Journal of Geophysical Research*, *70*(3), 733–738. https://doi.org/10.1029/JZ070i003p00733

Frissell, N. A. (2023). 2023 annular and 2024 total North American solar eclipse obscuration calculations [Dataset]. *Zenodo*. https://doi.org/10.5281/zenodo.7823585

Greenwald, R. A., Baker, K. B., Dudeney, J. R., Pinnock, M., Jones, T. B., Thomas, E. C., et al. (1995). DARN/SuperDARN: A global view of the dynamics of high-latitude convection. *Space Science Reviews*, *71*(1), 761–796. https://doi.org/10.1007/BF00751350

Greenwald, R. A., Baker, K. B., Hutchins, R. A., & Hanuise, C. (1985). An HF phased-array radar for studying small-scale structure in the high-latitude ionosphere. *Radio Science*, *20*(1), 63–79. https://doi.org/10.1029/RS020i001p00063

Grigorenko, E. I., Lyashenko, M. V., & Chernogor, L. F. (2008). Effects of the solar eclipse of March 29, 2006, in the ionosphere and atmosphere. *Geomagnetism and Aeronomy*, *48*(3), 337–351. https://doi.org/10.1134/S0016793208030092

Guo, Q., Chernogor, L. F., Garmash, K. P., Rozumenko, V. T., & Zheng, Y. (2020). Radio monitoring of dynamic processes in the ionosphere over China during the partial solar eclipse of 11 August 2018. *Radio Science*, *55*(2), e2019RS006866. https://doi.org/10.1029/2019RS006866

Hanuise, C., Broche, P., & Ogubazghi, G. (1982). HF Doppler observations of gravity waves during the 16 February 1980 solar eclipse. *Journal of Atmospheric and Terrestrial Physics*, *44*(11), 963–966. https://doi.org/10.1016/0021-9169(82)90060-5

Jakowski, N., Stankov, S. M., Wilken, V., Borries, C., Altadill, D., Chum, J., et al. (2008). Ionospheric behavior over Europe during the solar eclipse of 3 October 2005. *Journal of Atmospheric and Solar-Terrestrial Physics*, *70*(6), 836–853. https://doi.org/10.1016/j.jastp.2007.02.016

Jones, T. B., Wright, D. M., Milner, J., Yeoman, T. K., Reid, T., Chapman, P. J., & Senior, A. (2004). The detection of atmospheric waves produced by the total solar eclipse of 11 August 1999. *Journal of Atmospheric and Solar-Terrestrial Physics*, *66*(5), 363–374. https://doi.org/10.1016/j.jastp.2004.01.029

Kunduri, B. S. R., Baker, J. B. H., Ruohoniemi, J. M., Thomas, E. G., Huba, J. D., Emmons, D. J., et al. (2024). HF radar observations and modeling of the impact of the 8 April 2024 total solar eclipse on the ionosphere-thermosphere system. *Geophysical Research Letters*, *51*, e2024GL112484. https://doi.org/10.1029/2024GL112484

Le, H., Liu, L., Yue, X., & Wan, W. (2008). The midlatitude F2 layer during solar eclipses: Observations and modeling. *Journal of Geophysical Research*, *113*(A8), A08309. https://doi.org/10.1029/2007JA013012

Moses, M. L., Kordella, L. J., Earle, G. D., Drob, D., Huba, J. D., Ruohoniemi, J. M., et al. (2021). Observations and modeling studies of solar eclipse effects on oblique high frequency radio propagation. *Space Weather*, *19*(3), e2020SW002560. https://doi.org/10.1029/2020SW002560

Mosna, Z. J. B., Koucka Knizova, P., Sindelarova, T., Kouba, D., Chum, J., et al. (2018). Observation of the solar eclipse of 20 March 2015 at the Pruhonice station. *Journal of Atmospheric and Solar-Terrestrial Physics*, *171*, 277–284. https://doi.org/10.1016/j.jastp.2017.07.011

Müller-Wodarg, I. C. F., Aylward, A. D., & Lockwood, M. (1998). Effects of a mid-latitude solar eclipse on the thermosphere and ionosphere—A modelling study. *Geophysical Research Letters*, *45*(20), 3319–3327. https://doi.org/10.1029/1998GL900045

Nishitani, N., Ruohoniemi, J. M., Lester, M., Baker, J. B. H., Koustov, A. V., Shepherd, S. G., et al. (2019). Review of the accomplishments of mid-latitude Super Dual Auroral Radar Network (SuperDARN) HF radars. *Progress in Earth and Planetary Science*, *6*(1), 27. https://doi.org/10.1186/s40645-019-0270-5

Panasenko, S. V., Otsuka, Y., van de Kamp, M., Chernogor, L. F., Shinbori, A., Tsugawa, T., & Nishioka, M. (2019). Observation and characterization of traveling ionospheric disturbances induced by solar eclipse of 20 March 2015 using incoherent scatter radars and GPS networks. *Journal of Atmospheric and Solar-Terrestrial Physics*, *191*, 105051. https://doi.org/10.1016/j.jastp.2019.05.015

Reinisch, B. W., & Galkin, I. A. (2011). Global ionospheric radio observatory (GIRO). *Earth Planets and Space*, *63*(4), 377–381. https://doi.org/10.5047/eps.2011.03.001

Ribeiro, A. J., Ruohoniemi, J. M., Ponomarenko, P. V., Clausen, L. B. N., Baker, J. B. H., Greenwald, R. A., et al. (2013). A comparison of SuperDARN ACF fitting methods. *Radio Science*, *48*(3), 274–282. https://doi.org/10.1002/rds.20031

Rishbeth, H. (1968). Solar eclipses and ionospheric theory. *Space Science Reviews*, *8*(4), 543–554. https://doi.org/10.1007/BF00175006

Salah, J. E., Oliver, W. L., Foster, J. C., Holt, J. M., Emery, B. A., & Roble, R. G. (1986). Observations of the May 30, 1984, annular solar eclipse at Millstone Hill. *Journal of Geophysical Research*, *91*(A2), 1651–1660. https://doi.org/10.1029/JA091iA02p01651

Sindelarova, T., Mosna, Z., Chum, J., Kouba, D., Base, J., Liu, J. Y., & Katamzi-Joseph, Z. (2018). Solar eclipse effects in the ionosphere observed by continuous Doppler sounding. *Journal of Atmospheric and Solar-Terrestrial Physics*, *62*(4), 785–800. https://doi.org/10.1016/j.asr.2018.05.029

SuperDARN Data Analysis Working Group, Thomas, E. G., Reimer, A. S., Bland, E. C., Burrell, A. G., Grocott, A., et al. (2022). SuperDARN Radar Software Toolkit (RST) 5.0 [Software]. *Zenodo*. https://doi.org/10.5281/zenodo.7467337

Thomas, E. G., & Shepherd, S. G. (2022). Virtual height characteristics of ionospheric and ground scatter observed by mid-latitude SuperDARN HF radars. *Radio Science*, *57*(6), e2022RS007429. https://doi.org/10.1029/2022RS007429

Thomas, E. G., Shepherd, S. G., Kunduri, B. S. R., & Themens, D. R. (2024). Data set for Multi-frequency SuperDARN HF radar observations of the ionospheric response to the October 2023 annular solar eclipse [Dataset]. *Zenodo*. https://doi.org/10.5281/zenodo.13742779

Vertogradov, G. G., & Vertogradova, E. G. (2016). The investigation of ionospheric response to total eclipses on 29th March, 2006 and on 20th March, 2015 based on HF oblique sounding data. *Journal of Atmospheric and Solar-Terrestrial Physics*, *147*, 28–36. https://doi.org/10.1016/j.jastp.2016.06.013

Zhang, S.-R., Erickson, P. J., Goncharenko, L. P., Coster, A. J., Rideout, W., & Vierinen, J. (2017). Ionospheric bow waves and perturbations induced by the 21 August 2017 solar eclipse. *Geophysical Research Letters*, *44*(12), 067–073. https://doi.org/10.1002/2017GL076054

19448007, 2024, 24, Downloaded from https://agupubs.onlinelibrary.wiley.com/doi/10.1029/2024GL112450, Wiley Online Library on [12/12/2024]. See the Terms and Conditions (https://onlinelibrary.wiley.com/terms-and-conditions) on Wiley Online Library for rules of use; OA articles are governed by the applicable Creative Commons License